RSC Advances

PAPER

View Article Online
View Journal | View Issue

Cite this: *RSC Adv.*, 2026, **16**, 29529

Harnessing wetting transitions to program dual-mode antibacterial textiles

Sujin Jeong,[a] Kyeongeun Lee,[b] Sebin Lee[a] and Jooyoun Kim *[ac]

Anti-biofouling and antimicrobial treatments often face intrinsic trade-offs between short-term surface repellence and long-term bactericidal activity. Herein, a time-sequenced dual-defense textile platform is presented based on Cu/Zn bimetallic imidazolate frameworks grown on cotton fabrics *via* a composition-controlled coordinating strategy and vacuum-assisted pore activation. In particular, this work introduces a materials-design concept in which interfacial wetting dynamics are deliberately exploited to program sequential functionality. The pore-activated metal–organic framework surface initially stabilizes trapped air pockets, imparting superhydrophobicity and suppressing bacterial adhesion. Upon prolonged exposure to bacterial suspension, pore wetting occurs, triggering interactions between bacteria and reactive oxygen species of $^{\bullet}O_2^-$ and $^{\bullet}OH$, generated through Cu^+/Cu^{2+} redox cycling. This transition induces intracellular oxidative stress in *Escherichia coli*, as confirmed by assays. Systematic tuning of the Cu/Zn ratio grants control over the balance between anti-adhesive persistence and bactericidal potency, where Cu-rich frameworks achieve a bactericidal efficiency of 99.2% after 120 min, suitable for high-risk clinical environments, while Zn-rich compositions extend the anti-adhesive state for daily-wear applications. This study advances a dynamic, wetting-regulated materials principle that allows adaptive antibacterial performance, offering a broadly applicable strategy for hygiene textiles, with immediate bacterial repulsion and sustained oxidative inactivation.

Received 7th March 2026
Accepted 26th May 2026

DOI: 10.1039/d6ra01949h

rsc.li/rsc-advances

1. Introduction

Antibacterial textiles have attracted significant attention in public health and clinical care with their ability to inhibit bacterial proliferation and mitigate the spread of infectious diseases.[1,2] Given that textile materials are continually exposed to microbial contamination across various daily settings, bacterial adhesion and subsequent colonization on their surfaces can pose serious risks.[3,4] These risks extend beyond compromised hygiene and malodor generation to a significantly increased likelihood of cross-infection, particularly in high-stakes environments.[5] To mitigate these risks, extensive efforts have focused on imparting antibacterial functionality to textiles, primarily through two strategies: (i) bactericidal approaches that employ active agents to kill bacteria,[6–9] and (ii) anti-adhesion approaches that prevent bacterial attachment to the substrate.[10,11] However, integrating both functions within a single platform remains challenging, as low surface energy coatings required for anti-adhesion may obscure or deactivate the active sites necessary for effective disinfection.[12–14] Despite this inherent trade-off, a dual-mechanism strategy is crucial for comprehensive protection. Specifically, anti-adhesion is critical for preventing initial contamination, whereas potent bactericidal activity is required to eradicate bacteria that eventually adhere over time or as the surface's repellency deteriorates.[15–17]

Anti-adhesion strategies predominantly focus on engineering superhydrophobic surfaces, either by mimicking the hierarchical micro/nano-roughness of the lotus leaf or by lowering surface energy through chemical modification to minimize bacterial residence time.[18–20] It is well established that such surfaces, characterized by apparent contact angles exceeding 150° and roll-off angles below 10°,[20–22] effectively suppress initial bacterial adhesion and inhibit biofilm formation.[23] However, the practical effectiveness of anti-adhesion surfaces often deteriorates due to wetting transitions under prolonged liquid exposure or organic fouling.[15] An alternative approach, disinfection-oriented functionalization, relies on antibacterial metal ions (*e.g.*, Ag, Cu)[24–26] or photocatalysts to induce direct cellular damage and eradicate bacteria attached to the substrate.[27–29]

While it is ideal to integrate both bactericidal and anti-adhesive functionalities, a critical limitation arises when low surface energy coatings are employed, as these layers can passivate the surface and act as physical barriers that impede the diffusion of active bactericidal agents such as reactive oxygen species (ROS), thereby compromising bactericidal

[a]*Department of Fashion and Textiles, Seoul National University, Seoul 08826, Republic of Korea. E-mail: jkim256@snu.ac.kr*

[b]*Industry & Business Support Center, FITI Testing & Research Institute, Seoul 07791, Republic of Korea*

[c]*Research Institute of Human Ecology, Seoul National University, Seoul, 08826, Republic of Korea*

efficacy.[13] Meanwhile, disinfection-only approaches fail to prevent initial bacterial attachment, promoting the formation of biofilms that eventually shield bacteria from the underlying treatment. Additionally, many photocatalytic systems are inherently limited by their reliance on external light sources, which restricts their applicability in real-world conditions.[30] For these reasons, studies that concurrently integrate superhydrophobic anti-adhesion and light-independent, ROS-mediated disinfection within a single textile platform are scarce.

To address these challenges and achieve the dual-defense against bacterial contamination, metal–organic frameworks (MOFs) featuring Cu–N coordination sites, particularly within the zeolitic imidazolate framework (ZIF) family, are employed as a multifunctional platform. Specifically, we construct a dual-mode protective interface that initially repels bacteria through superhydrophobicity and subsequently eliminates adhered bacteria *via* localized generation of ROS. Persistent, light-independent ROS production is achieved by partially substituting Zn with Cu in the imidazolate framework, leveraging continuous Cu^{+}/Cu^{2+} redox cycling.[31,32] The Cu/Zn imidazolate frameworks grown on fabric imparts nanoscale roughness to the surface, while a subsequent pore-activation process establishes stable air pockets within the MOF architecture. This air-trapping layer effectively minimizes the solid–liquid contact area, inducing a superhydrophobic state where droplets remain suspended on the surface.[33,34] Importantly, unlike conventional polymer-based coatings, this activation-based approach preserves access to ROS-generating active sites, allowing a seamless integration of anti-adhesion and bactericidal functions.

The novelty of this work lies in the engineering of a time-sequenced dual defense system that synergistically couples short-term physical anti-adhesion with long-term, ROS-mediated sterilization. Through pore activation, the inherent performance trade-offs of conventional hygienic materials are effectively decoupled. Notably, the wetting transition is reinterpreted not as a failure mode but as a functional trigger that activates latent bacterial protection, ensuring sustained antimicrobial efficacy even after the surface becomes fully wetted. Furthermore, the Cu/Zn ratio was identified as a pivotal design parameter governing crystalline phase evolution, ROS generation efficiency, and wetting-transition kinetics. By tuning this ratio, the dominant antibacterial mechanism can be modulated to accommodate varying contamination levels and environmental conditions. This study conceives a novel approach for designing adaptive, high-performance hygienic textiles with long-term functional stability.

2. Experimental methods

2.1 Synthesis of ZIF-L and Cu/Zn bimetallic imidazolate framework on cotton

For ZIF-L synthesis on fabrics, cotton fabrics (3 cm × 3 cm) were first immersed in a 25 mM of zinc nitrate hexahydrate ($Zn(NO_3)_2 \cdot 6H_2O$) solution at room temperature for 30 min, after which 250 mM of 2-methylimidazole (2-mIm) solution was added to achieve a Zn : 2-mIm molar ratio of 1 : 10 in the reaction system, with the metal ion amount fixed at 1 mmol. The reaction mixture was kept at room temperature for 24 h, and then the treated fabrics were washed three times with distilled water. To activate the internal pores of the ZIF-L, the samples were dried overnight at 100 °C under vacuum, and the resulting sample was denoted as ZIF-L_{act}. For comparison, ZIF-L grown fabrics were also dried at room temperature for 24 h without vacuum treatment to purposely maintain unactivated pores, and the resulting sample was denoted as ZIF-L_{un}.

Cu/Zn imidazolate on cotton was synthesized under the same conditions except that 12.50 mM or 18.75 mM of copper(II) nitrate trihydrate ($Cu(NO_3)_2 \cdot 3H_2O$) was introduced into the 12.50 mM or 6.25 mM of zinc nitrate solution, to obtain Cu : Zn molar ratios of 1 : 1 or 3 : 1, while maintaining the total metal ion amount constant at 1 mmol. The resulting fabrics were denoted as Cu : Zn$[1:1]_{un}$, Cu : Zn$[3:1]_{un}$ (atmospheric drying at room temperature), Cu : Zn$[1:1]_{act}$, and Cu : Zn$[3:1]_{act}$ (activated by vacuum drying at 100 °C), depending on the pore-activation. After preparation, activated samples were stored in an oven at 80 °C to prevent moisture uptake, whereas unactivated samples were stored in sealed plastic zipper bags at room temperature (25 °C). All wettability characterizations were performed within 1 day after sample preparation.

2.2 Bactericidal activity evaluation based on ATP and PI assay

Escherichia coli (*E. coli*) was cultured to the logarithmic phase and diluted to 2×10^8 colony-forming units per mL (CFU mL^{-1}). Fabric specimens (1 cm × 1 cm) were immersed in 700 μL of the bacterial suspension in sealed microtubes. The suspension volume was sufficient to maintain the fabric specimens fully immersed throughout the incubation period. The samples were then incubated at 37 °C for 1, 15, 30, 60, and 120 min. Following the incubation, the fabrics were removed, and the remaining suspension was centrifuged at 6000 rpm for 5 min. The resulting pellet was resuspended in phosphate-buffered saline (PBS) and divided into two aliquots for ATP-based viability assay and propidium iodide (PI) staining assay. The ATP assay was performed using a BacTiter-Glo™ Microbial Cell Viability Assay Kit (Promega, USA). The bacterial suspension was mixed with BacTiter-Glo reagent and incubated in the dark at room temperature for 5 min. Luminescence was measured using a multimode microplate reader (BioTek Instruments, USA).

The second aliquot of the supernatant was used for the PI staining assay to quantify dead cells. PI ($\lambda_{ex} = 490$ nm, $\lambda_{em} = 635$ nm) was added to the bacterial suspension and incubated for 12 min at room temperature, and red fluorescence intensity generated by the dead cell bound to PI was measured using the multimode microplate reader equipped for fluorescence detection.

The bactericidal efficiency (%) was calculated based on the ATP assay results using eqn (1), where C represents the luminescence intensity of viable bacteria after incubation with the fabric sample for a given time, and C_0 represents that obtained

from pristine cotton fabric without Cu/Zn imidazolate, used as the substrate control. In addition, an '*E. coli* only' group without fabric was included as a bacterial growth control.

$$\text{Bactericidal efficiency}(\%) = \frac{C_0 - C}{C_0} \times 100 \quad (1)$$

2.3 Assessment of ROS-induced intracellular oxidative stress

Intracellular oxidative stress in *E. coli* cells was evaluated to identify sub-lethally damaged cells. ROS-induced oxidative stress was analyzed using 2′,7′-dichlorodihydrofluorescein diacetate (DCFH-DA) as a ROS-sensitive fluorescent probe. After incubation with fabric specimens for 30 min, the *E. coli* suspension was centrifuged at 6000 rpm for 5 min, and the pellet was resuspended in PBS. The resuspended cells were then incubated with DCFH-DA for 30 min in the dark. The fluorescence intensity (λ_{ex} = 488 nm, λ_{em} = 500 nm) was measured using a multimode microplate reader.

2.4 Quantification of live and dead cells attached to the fabric surface

Bacterial adhesion and viability on the fabric surface were examined using *E. coli* suspensions prepared as described above. After incubation, fabric specimens were gently rinsed with PBS to remove loosely attached cells. Adherent bacteria were detached by immersing each fabric in 700 μL of extraction buffer (0.1 mM ethylenediaminetetraacetic acid and 0.05% Tween 80 in PBS) followed by three sonication cycles (10 s each), with 20 s cooling intervals on ice between cycles. The resulting suspensions were allowed to stand for 10 min to sediment solid residues, and the supernatants were collected for viability analysis. To quantify live-cells, 100 μL of the extract was transferred into a 96-well microplate, supplemented with $MgCl_2$ to a final concentration of 5 mM, mixed with an equal volume (100 μL) of ATP assay reagent, and incubated in the dark for 5 min. Dead-cell analysis was performed by mixing 100 μL of the extract with an equal volume of PI solution, followed by incubation in the dark for 15 min. ATP-derived luminescence (for viable cells) and PI fluorescence (for dead cells) intensities were then measured using a multimode microplate reader under respective detection modes. For each sample type, five independently prepared fabric specimens were tested. The data are presented as means, and the error bars represent the corresponding standard deviations. The luminescence and fluorescence intensity were converted into bacterial concentration (CFU cm^{-2}) using a calibration curve, as described in Fig. S7. The recovery efficiency of the bacterial extraction process was additionally evaluated and is presented in Fig. S9. In addition, the effect of the sonication-ice cooling cycles on *E. coli* viability was also independently verified and is presented in Fig. S10.

2.5 Evaluation of bactericidal activity after repeated washing cycles

To evaluate the functional durability of the Cu/Zn imidazolate fabrics under repeated use conditions, bactericidal activity was assessed across five successive test cycles for Cu : Zn$[1:1]_{un}$ and Cu : Zn$[3:1]_{un}$. After each bactericidal activity test, the fabric specimens were washed by immersion in 200 mL of distilled water at room temperature (25 °C) under stirring at 150 rpm for 3 min, then air-dried at room temperature for 30 min. Bactericidal activity was then re-evaluated using the identical protocol described in the 'Experimental methods' section. This procedure was repeated to yield a total of five test cycles: one prior to any washing (no wash) and four successive washing–testing cycles. For each test cycle, three independently prepared fabric specimens were used. The data are presented as means, and the error bars represent the corresponding standard deviations.

3. Results and discussion

3.1 Characteristics of Cu/Zn bimetallic imidazolate frameworks on fabrics

The morphologies of the Cu/Zn bimetallic imidazolate frameworks grown on the fibers were examined to understand the influence of the Cu/Zn feeding ratio on the evolution of crystal morphology (Fig. 1a–c), with pristine cotton fabric shown in Fig. S1. The Zn-based imidazolate structures exhibited the characteristic leaf-like morphology of ZIF-L, which remained consistent regardless of pore activation (Fig. S2). In the bimetallic imidazolate, Cu : Zn$[1:1]_{act}$ (synthesized with a 1 : 1 molar feeding ratio of Cu to Zn), exhibited a crystalline morphology similar to that of ZIF-L. The particle dimensions of Cu : Zn$[1:1]_{act}$ were 5.1 ± 2.3 μm in length and 1.3 ± 0.5 μm in width, comparable to those of the pristine ZIF-L, which were 5.5 ± 2.8 μm in length and 1.4 ± 0.8 μm in width. In contrast, the Cu : Zn $[3:1]_{act}$ displayed hierarchical, flower-like architectures composed of radially oriented hexagonal nanosheets, with an aggregate diameter of about 22.5 ± 2.7 μm. For Cu : Zn$[3:1]$, since Cu^{2+} ions exhibit a lower binding affinity toward 2-mIm ligands than Zn^{2+} ions, an excessive Cu concentration reduces the density of nucleation sites and prolongs the crystal growth phase.[31,35] This kinetic shift facilitates the formation of significantly larger and more complex crystalline structures.

Energy-dispersive spectroscopy (EDS) elemental mapping in Fig. 1d confirms the successful incorporation of both Cu and Zn species in Cu/Zn imidazolate frameworks on the fiber surface. Also, EDS analysis revealed that the actual Cu/Zn atomic ratios in the grown structures differed from the precursor feed ratios. Although Cu : Zn ratios of 1 : 1 and 3 : 1 were used during synthesis, the corresponding Cu/Zn atomic ratios determined from EDS were 0.30 ± 0.03 and 2.06 ± 0.14, respectively. These discrepancies originate from differences in the coordination chemistry and nucleation behavior of Zn^{2+} and Cu^{2+} ions. As Zn^{2+} ions exhibit stronger coordination affinity toward 2-mIm ligands, this promotes more rapid ligand deprotonation, facilitating faster Zn-imidazolate coordination.[36] As a result, particularly at lower Cu^{2+} feed ratios, the incorporation of Cu^{2+} is kinetically limited, yielding final compositions deviating from the precursor feeding ratios. This interpretation is corroborated by inductively coupled plasma-atomic emission spectroscopy (ICP-AES) measurements (Fig. S3), showing that Zn^{2+} ions are consumed at a significantly faster rate than Cu^{2+}

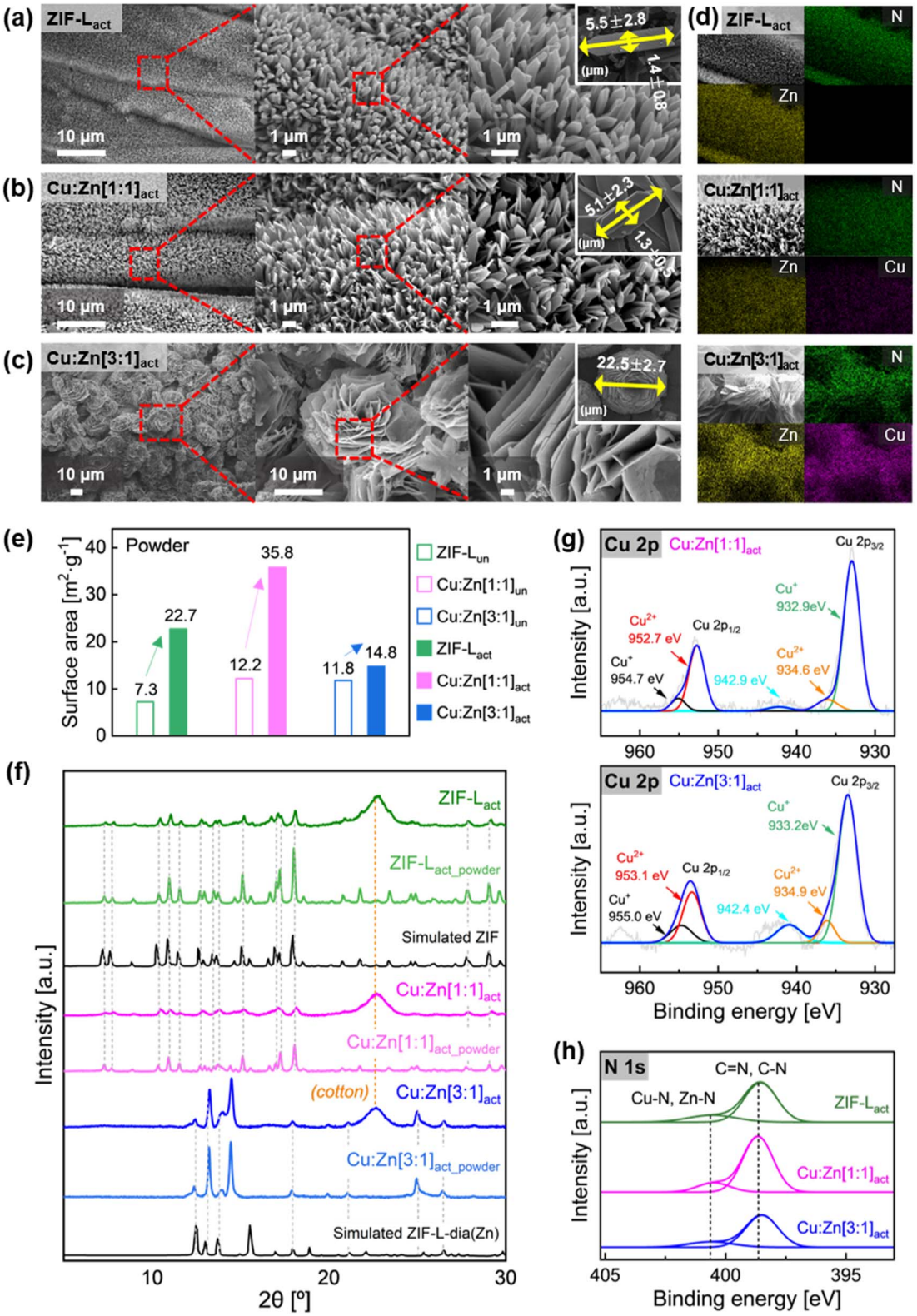

Fig. 1 Characterization of Cu/Zn imidazolate and ZIF-L grown on fibers. SEM images of (a) ZIF-L_{act}, (b) Cu : Zn[1 : 1]$_{act}$, and (c) Cu : Zn[3 : 1]$_{act}$ and (d) corresponding EDS elemental mapping. (e) BET surface area of ZIF-L, Cu : Zn[1 : 1], and Cu : Zn[3 : 1] measured in powder form before and after activation. (f) XRD patterns of ZIF-L_{act}, Cu : Zn[1 : 1]$_{act}$ and Cu : Zn[3 : 1]$_{act}$ with simulated ZIF-L and ZIF-dia(Zn).[37] XPS spectra of (g) Cu 2p and (h) N 1s.

ions during the early stages of growth in the solution. Pore activation of the synthesized MOFs was conducted to remove residual solvent confined within the imidazolate pores. From Fig. 1e, the Brunauer–Emmett–Teller (BET) surface areas measured from the MOF powders showed that all activated samples (ZIF-L_{act}, Cu : Zn[1 : 1]$_{act}$, and Cu : Zn[3 : 1]$_{act}$) exhibited higher BET surface areas than the unactivated samples (ZIF-L_{un}, Cu : Zn[1 : 1]$_{un}$, and Cu : Zn[3 : 1]$_{un}$), indicating effective removal of residual moisture from the pore interiors. The BET surface areas measured from the MOF-grown fabric samples are additionally provided in Fig. S4. This pore activation did not alter the crystal morphologies observed by field-emission scanning electron microscopy (FE-SEM) or high-resolution X-ray diffraction (XRD), nor did it affect the elemental composition determined by EDS.

As shown in Fig. 1f of XRD analysis, the diffraction patterns of ZIF-L_{act} and Cu : Zn[1 : 1]$_{act}$ closely match the simulated ZIF-L structure,[37,38] confirming the preservation of the ZIF-L framework. In contrast, Cu : Zn[3 : 1]$_{act}$ exhibits distinct diffraction peaks at 12.4°, 12.9°, and 13.6°, corresponding to the ZIF-dia phase, a polymorph related to ZIF-8 with a hexagonal nanosheet structure.[39,40] Notably, these peaks are shifted toward higher 2θ values compared with pristine ZIF-dia, indicating reduced interplanar spacing. This rightward shift suggests partial substitution of Zn^{2+} ions by Cu^{2+} ions within the imidazolate lattice, attributed to the smaller effective ionic radius of Cu^{2+} (0.57 Å) relative to Zn^{2+} (0.60 Å).[41] The appearance of new diffraction features at 14.5° further indicates the formation of a hierarchical, flower-like morphology distinct from the planar ZIF-dia structure.

X-ray photoelectron spectrometer (XPS) spectra in Fig. 1g and h reveal the mixed-valence Cu species and metal–ligand coordination. The Cu 2p spectra (Fig. 1g) display characteristic peaks of Cu^{2+} (934.6–934.9 eV) and Cu^{+} (932.9–933.2 eV), indicating the coexistence of mixed-valence copper species. In the N 1s region (Fig. 1h), signals at 398.5 eV (C=N, C–N) and 400.8 eV (metal–N coordination) verify imidazolate binding to both Cu and Zn. The presence of mixed-valence Cu species coordinated through N atoms suggests the formation of Cu–N sites, which are known to facilitate electron transfer processes and may serve as redox-active centers relevant to the ROS generation.[31,33,41]

The mass loading of the imidazolates on the textile substrate was estimated by thermogravimetric analysis (TGA) (Fig. S5) to be 16.2% for ZIF-L, 18.6% for Cu : Zn[1 : 1], and 27.9% for Cu : Zn[3 : 1], indicating higher MOF loadings as the Cu precursor contents increased. Overall, the morphological and spectroscopic results demonstrate that varying the Cu/Zn feeding ratio effectively tunes the composition and crystalline structure of the synthesized MOFs, while the pore activation does not alter the underlying structural chemical characteristics.

3.2 Wettability of Cu/Zn imidazolate fabrics

The MOF pores were activated by vacuum drying to remove residual solvents and trapped moisture from the ZIF-L and Cu/Zn imidazolate crystal pores and interstitial spaces, thereby enhancing air retention within the MOF crystals. As the treated MOFs display a hydrophobic nature, the air pockets on the MOF surface augment the anti-wettability by reducing the contact area of the liquid. As a result, the samples exhibited distinct surface wettability depending on the pore activation, despite having identical crystal morphologies.

The wettability of the Cu/Zn imidazolate fabric was evaluated by measuring the static contact angle (CA) and shedding angle (SA) of water and Luria–Bertani (LB) broth. As shown in Fig. 2a, the unactivated samples (ZIF-L_{un}, Cu : Zn[1 : 1]$_{un}$, Cu : Zn[3 : 1]$_{un}$) exhibited complete wetting behavior, with liquid droplets immediately spreading across the fabric surface (CA $\approx$ 0°) (Video S1). In contrast, the activated samples (ZIF-L_{act}, Cu : Zn[1 : 1]$_{act}$, Cu : Zn[3 : 1]$_{act}$) displayed superhydrophobicity, with CAs approaching 179° for both water and LB broth (Fig. 2b). The nonadherent nature of the activated surfaces was further observed in Fig. 2c and Video S2; when liquid droplets were brought into contact with the surfaces of ZIF-L_{act}, Cu : Zn[1 : 1]$_{act}$, and Cu : Zn[3 : 1]$_{act}$, the droplets failed to adhere and readily detached upon contact, demonstrating the strong water repellency. This repellency was also corroborated by small SAs, where SAs of water were: 6.4 $\pm$ 0.6° for ZIF-L_{act}, 6.1 $\pm$ 0.5° for Cu : Zn[1 : 1]$_{act}$, and 6.8 $\pm$ 0.7° for Cu : Zn[3 : 1]$_{act}$, while SAs of LB broth were: 7.1 $\pm$ 0.7° for ZIF-L_{act}, 6.6 $\pm$ 0.4° for Cu : Zn[1 : 1]$_{act}$, and 7.3 $\pm$ 0.6° for Cu : Zn[3 : 1]$_{act}$ (Fig. 2d).

Despite their pronounced superhydrophobicity, the activated samples gradually transitioned to a wetted state during prolonged exposure to liquid environments. The time-dependent evolution of the CA is presented in Fig. 2e for water and LB broth, respectively. For water, the contact angle decreased below 150° after approximately 25 min for ZIF-L_{act}, 60 min for Cu : Zn[1 : 1]$_{act}$, and 40 min for Cu : Zn[3 : 1]$_{act}$. In LB broth, the wetting transition occurred more rapidly, with CA decrease observed below 150° after approximately 10 min for ZIF-L_{act}, 33 min for Cu : Zn[1 : 1]$_{act}$, and 17 min for Cu : Zn[3 : 1]$_{act}$. This wettability transition is attributed to the gradual infiltration of liquid into the micro/nano-pores and interstitial void spaces of the textured surface, where air was initially trapped after activation, leading to progressive displacement of the trapped air and a corresponding increase in the solid–liquid contact area.[13] The wetting transition occurred more rapidly in LB broth than in water, primarily due to its lower surface tension (56.6 mN m^{-1}) relative to water (72.7 mN m^{-1}) that facilitated capillary intrusion into the micro/nanopores. The Cu : Zn[3 : 1]$_{act}$ exhibited a faster wetting progression than Cu : Zn[1 : 1]$_{act}$.

This wettability transition, in turn, enhances the accessibility of the bacterial suspension to the surface, leading to two contrasting effects on bacterial proliferation. On one hand, greater surface accessibility generally promotes bacterial attachment. On the other hand, for ROS-active surfaces, increased bacterial contact facilitates bactericidal activity. These seemingly contradictory roles of enhanced wettability are examined in the following section, which evaluates how wettability and ROS-generating capability collectively govern the overall antibacterial performance of the Cu/Zn imidazolate fabrics.

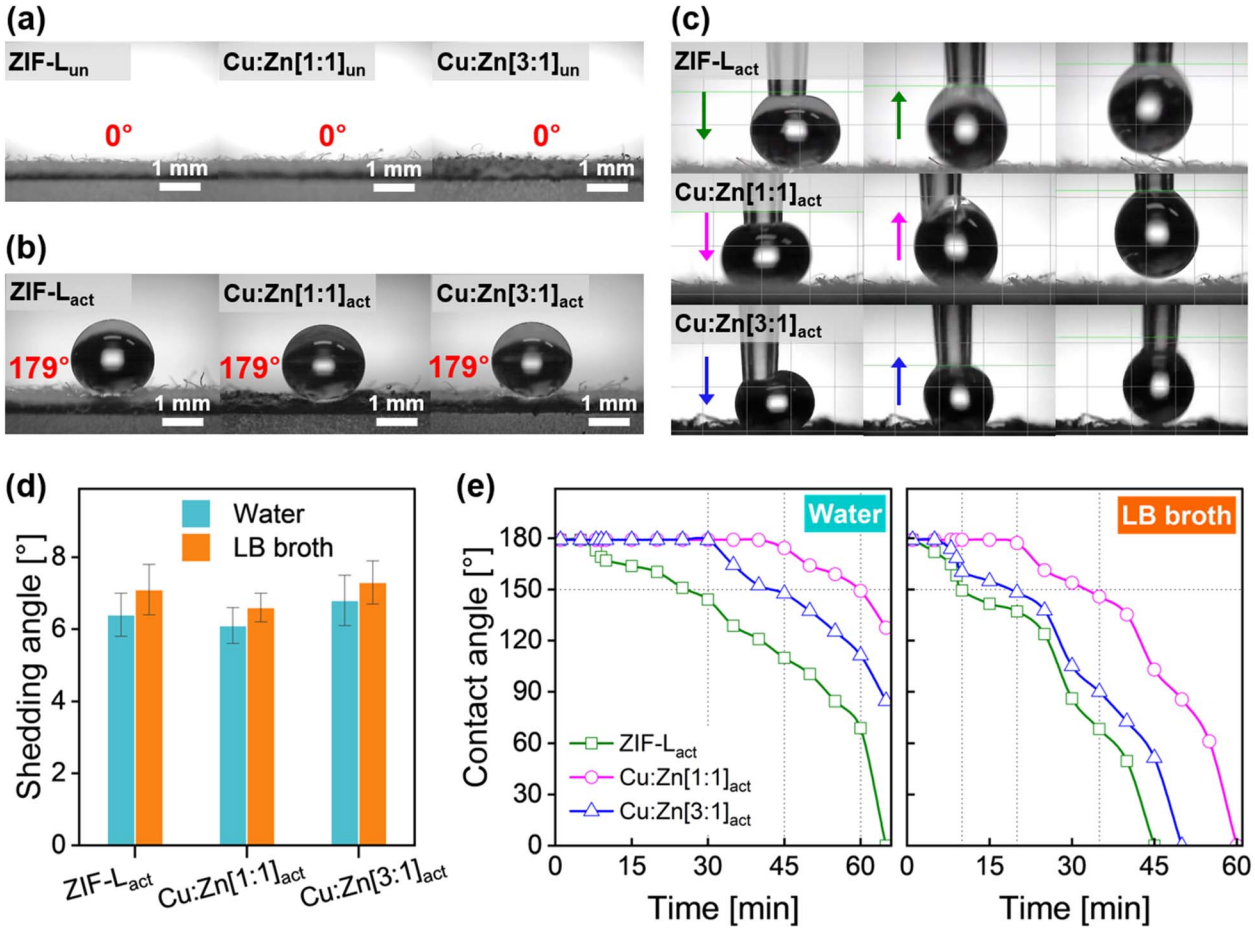

Fig. 2 Contact angles of (a) unactivated and (b) activated samples. (c) Non-adherent liquid droplets on ZIF-L_{act}, Cu : Zn[1 : 1]$_{act}$ and Cu : Zn[3 : 1]$_{act}$. (d) Shedding angles of water and LB droplets. (e) Contact angle evolution with time for activated Cu/Zn imidazolate fabrics for water and LB droplets.

3.3 ROS generation by Cu/Zn imidazolate frameworks

The ROS generation capability for ZIF-L, Cu : Zn[1 : 1], and Cu : Zn[3 : 1] was evaluated to compare the effect of Cu-induced redox activity and pore activation. In particular, superoxide radical ($^{\bullet}O_2^-$) and hydroxyl radical ($^{\bullet}OH$) were examined, as they are key ROS associated with Cu-mediated redox processes and subsequent antibacterial functionality.[42] The $^{\bullet}O_2^-$ generation was quantified based on the reduction of *p*-nitroblue tetrazolium chloride (NBT) to formazan, which results in a decrease in absorbance at 260 nm.[41,43] The $^{\bullet}OH$ generation was evaluated using the methylene blue dihydrate (MB) degradation assay, in which $^{\bullet}OH$ oxidatively decomposes MB, leading to a decrease in absorbance at 665 nm.[44] Accordingly, the ratios of the initial to the residual absorbance values (I_o and I_t represent the initial absorbance and the absorbance at time t, respectively, for NBT and MB) were used to represent the relative $^{\bullet}O_2^-$ and $^{\bullet}OH$ generation, respectively.

As shown in Fig. 3a and b, all samples exhibited a gradual increase in ROS production over time, indicating continuous ROS formation. A pronounced influence of pore activation was observed for both $^{\bullet}O_2^-$ and $^{\bullet}OH$ generation. Unactivated samples (ZIF-L_{un}, Cu : Zn[1 : 1]$_{un}$, and Cu : Zn[3 : 1]$_{un}$) exhibited relatively high ROS concentration, attributed to easier access of water to redox-active sites of MOFs that facilitates ROS generation. Initially, the hydrophobic, activated samples (ZIF-L_{act}, Cu : Zn[1 : 1]$_{act}$, and Cu : Zn[3 : 1]$_{act}$) showed slightly lower $^{\bullet}O_2^-$ and $^{\bullet}OH$ concentrations due to the hindrance of water access to the redox sites. With time lapse, the solution gradually infiltrated the air pockets of MOFs, increasing both $^{\bullet}O_2^-$ and $^{\bullet}OH$ generation and release.

As the Cu incorporation increased, both $^{\bullet}O_2^-$ and $^{\bullet}OH$ releases were enhanced across all samples. The Cu : Zn[3 : 1] consistently showed higher ROS concentrations than Cu : Zn[1 : 1]. It should be noted that ZIF-L exhibited the least ROS generation capability, particularly with a negligible $^{\bullet}O_2^-$ generation. These results demonstrate that ROS generation is influenced by the Cu content in the imidazolate framework. The observed ROS generation capability can be explained by the Cu-mediated redox mechanism established in previous studies on Cu-doped imidazolate frameworks and Cu–N-based nanozyme systems (Fig. 3c),[31,32] where substitution of Zn–N units with Cu–N coordination sites increases the local electron density around Cu centers and facilitates reversible Cu^+/Cu^{2+} redox cycling as shown in eqn (2)–(4). In this process, Cu^+ transfers electrons to

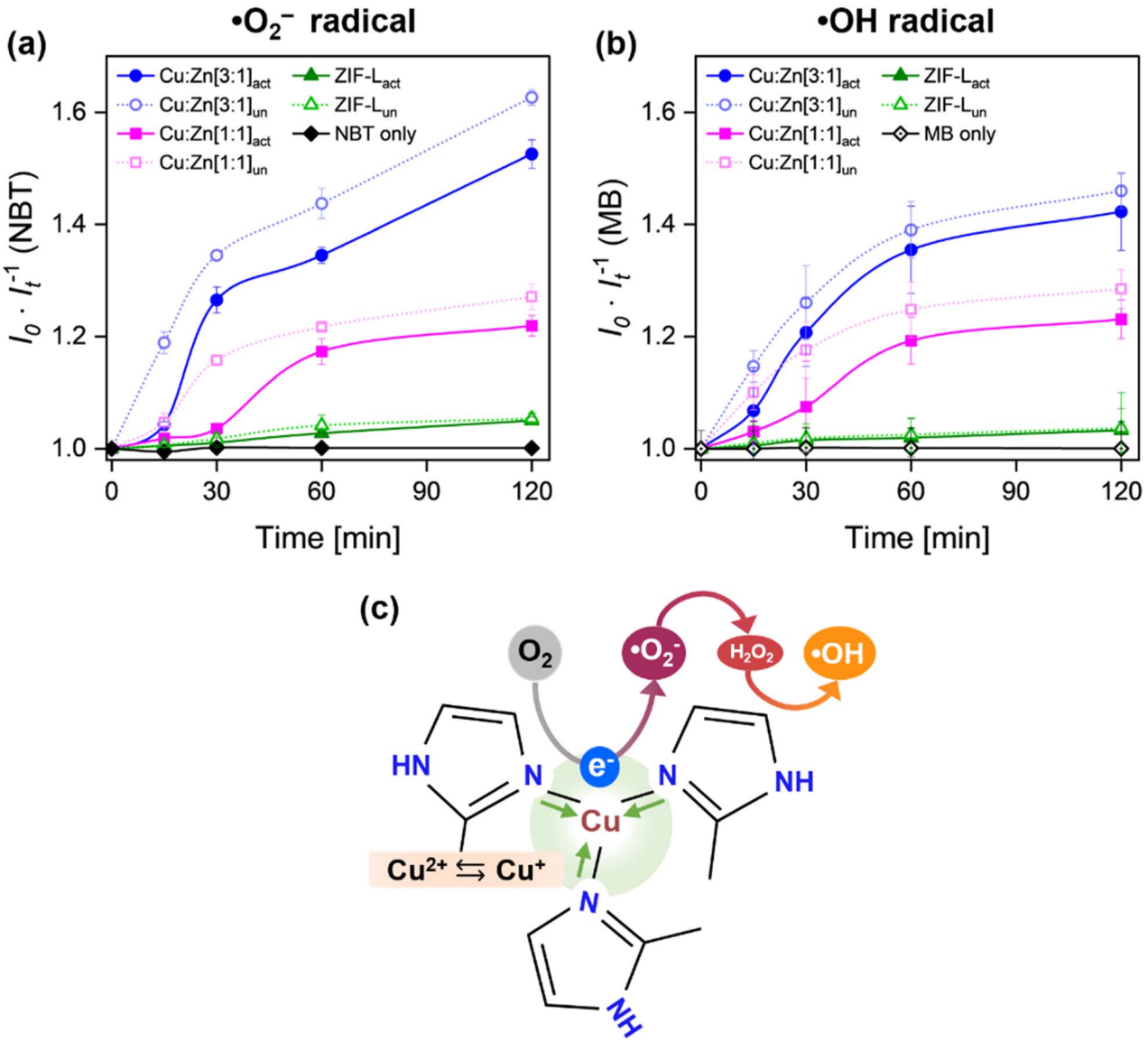

Fig. 3 Generation of (a) $^{\bullet}O_2^-$ and (b) $^{\bullet}OH$ radicals from Cu : Zn[3 : 1], Cu : Zn[1 : 1], and ZIF-L. (c) Schematic illustration of Cu–N coordinated active sites in Cu/Zn imidazolate mediating electron transfer and ROS formation.

oxygen to generate $^{\bullet}O_2^-$ (eqn (2)),[41] and the generated $^{\bullet}O_2^-$ undergoes disproportionation to form H_2O_2 (eqn (3)).[42,45] The H_2O_2 can further react with Cu^+ in a Fenton-like manner to produce highly reactive $^{\bullet}OH$ (eqn (4)).[46–48] Meanwhile, the oxidized Cu^{2+} species are reduced back to Cu^+ by accepting electrons from the reductive species, enabling sustained Cu^+/Cu^{2+} redox cycling.[49]

$$Cu^+ + O_2 + e^- \rightarrow Cu^{2+} + {}^{\bullet}O_2^- \quad (2)$$

$$2{}^{\bullet}O_2^- + 2H^+ \rightarrow H_2O_2 + O_2 \quad (3)$$

$$Cu^+ + H_2O_2 \rightarrow Cu^{2+} + {}^{\bullet}OH + OH^- \quad (4)$$

This cascade of reactions allows spontaneous and continuous ROS generation, and the efficiency of this process increases with the density of Cu–N active sites. Consequently, Cu-rich samples and surfaces with greater liquid accessibility exhibit enhanced ROS production, which directly underpins the antibacterial performance discussed below.

3.4 ROS-mediated bactericidal effect of MOF-grown fabrics in bacterial culture

Fig. 4a outlines a two-way approach for elucidating antibacterial defense mechanisms by evaluating the ROS-mediated bactericidal effects of Cu/Zn imidazolate framework-grown fabrics both in bacterial culture and at the fabric surface. In this section, bactericidal performance in a liquid-phase bacterial culture was investigated by immersing the MOF-grown fabrics in an *E. coli* culture. Fig. 4b and c present the number of both viable and dead cells, quantified by ATP-based luminescence and PI fluorescence assays, respectively. The ATP luminescence reflects intercellular ATP content through a luciferase-catalyzed

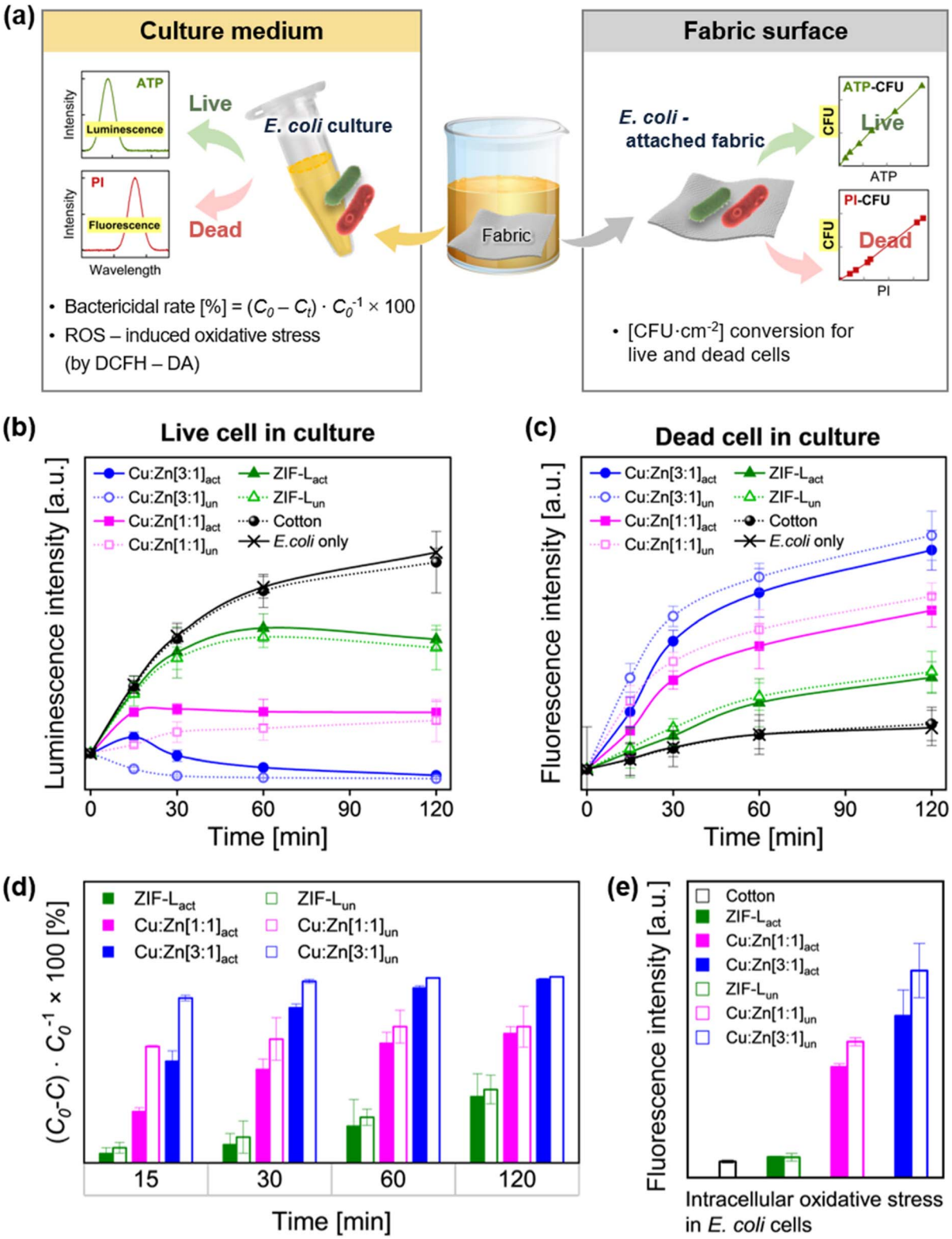

Fig. 4 (a) Schematic illustration of the experimental procedure for evaluating bactericidal activity in liquid culture and on the fabrics. (b) ATP luminescence and (c) PI fluorescence of *E. coli* in culture, representing viable and dead cell populations during incubation with fabric samples. (d) Bactericidal efficiency derived from ATP luminescence according to eqn (1). (e) Intracellular oxidative stress levels in *E. coli* cells after 30 min treatment with fabric, evaluated by DCFH-DA fluorescence.

reaction.[50] Based on the ATP-derived viability data in Fig. 4b, the bactericidal efficiency (%) was calculated and summarized in Fig. 4d.

As shown in Fig. 4b and c, the cotton fabric (control sample) exhibited a continuous increase in ATP luminescence intensity over time, comparable to that of the *E. coli* culture alone, indicating negligible bactericidal activity. Consistently, the PI fluorescence intensities of the cotton and *E. coli* culture alone remained relatively low throughout the incubation period, indicating minimal bacterial inactivation. ZIF-L fabrics also showed increasing ATP luminescence intensity with incubation time, although with a slightly reduced growth rate relative to the cotton fabric. Correspondingly, the PI fluorescence intensities of the ZIF-L samples increased only modestly, suggesting limited dead-cell accumulation. In contrast, Cu/Zn imidazolate fabrics exhibited substantially lower ATP luminescence intensities from the early stages of incubation, demonstrating effective suppression of bacterial proliferation. Simultaneously, the PI fluorescence intensities of the Cu/Zn imidazolate fabrics progressively increased with incubation time, indicating enhanced bacterial inactivation. Higher Cu incorporation and unactivated states resulted in more pronounced PI fluorescence intensities, consistent with their stronger bactericidal activity.

At the early incubation time of 15 min, vacuum-activated MOF-grown fabrics exhibited markedly lower bactericidal efficiencies (27.4% for Cu : Zn$[1:1]_{act}$ and 54.3% for Cu : Zn$[3:1]_{act}$) than their unactivated samples (62.2% for Cu : Zn$[1:1]_{un}$ and 87.8% for Cu : Zn$[3:1]_{un}$). This behavior is attributed to the air pockets trapped within the activated MOF, which effectively delays the contact between the bacterial suspension and the ROS-active sites, thereby limiting the interactions between ROS and bacteria in the liquid phase. With prolonged incubation, the bactericidal efficiencies of activated and unactivated samples gradually converge (Fig. 4d), indicating that progressive infiltration of the bacterial culture into the MOF structure enhances ROS accessibility and bactericidal action.

Overall, the bactericidal efficacy increased with higher Cu incorporation in the Cu/Zn imidazolate frameworks. ZIF-L_{act} exhibited limited activity, achieving 39.1% inactivation after 120 min, whereas the Cu : Zn$[1:1]_{act}$ showed a moderate response with a bactericidal efficiency of 68.9%. Cu : Zn$[3:1]_{act}$ consistently demonstrated the highest efficacy, reaching 97.7% after 120 min, highlighting the critical role of Cu content in governing bactericidal performance once sufficient liquid infiltration is established. Notably, the unactivated samples exhibited slightly higher bactericidal performance after 120 min incubation, reaching a maximum of 99.2% for Cu : Zn$[3:1]_{un}$. Extended incubation experiments up to 24 h further confirmed the long-term antibacterial performance of the Cu/Zn imidazolate fabrics. Bactericidal efficiencies for Cu : Zn$[3:1]_{act}$ and Cu : Zn$[3:1]_{un}$ reached nearly 100% after only 1 h of incubation, whereas Cu : Zn$[1:1]_{act}$ and Cu : Zn$[1:1]_{un}$ achieved nearly 100% bactericidal efficiency after 18 h, as shown in Fig. S6.

To confirm that the observed bactericidal activity originated from ROS generation, intracellular oxidative stress in *E. coli* was assessed using a DCFH-DA fluorescence assay after 30 min incubation (Fig. 4e). In this assay, intracellular ROS levels are quantified by the fluorescence intensity of dichlorofluorescein (DCF).[51,52] As shown in Fig. 4e, *E. coli* exposed to Cu/Zn imidazolate fabrics for 30 min exhibited markedly elevated fluorescence intensities compared to those treated with ZIF-L or cotton, indicating substantial intracellular ROS accumulation. Increased Cu incorporation led to stronger oxidative stress, and unactivated samples induced more pronounced effects than activated ones, consistent with enhanced ROS–bacteria interactions facilitated by enhanced wettability. The results demonstrate that direct contact between the ROS active sites and the bacterial suspension is important for effective bacterial inactivation, where bactericidal performance is primarily governed by the Cu content in Cu/Zn imidazolate frameworks and the surface wettability.

3.5 Bactericidal functional durability after repeated washing

The practical reusability of the Cu/Zn imidazolate fabrics was evaluated by assessing bactericidal activity across four successive washing–testing cycles (no washing through 4 washing cycles), each separated by a washing step. As shown in Fig. 5a, Cu : Zn$[1:1]_{un}$ exhibited stable antibacterial activity throughout all cyclic tests, with the bactericidal efficiency at 120 min decreasing from 72.6% of the initial sample without washing to 71.1% after 2-cyclic washing, and further to 68.6% after 4-cyclic washing, corresponding to a retention of over 94% of the initial performance. As shown in Fig. 5b, Cu : Zn$[3:1]_{un}$ demonstrated similarly well-preserved performance, with the 120 min bactericidal efficiency decreasing gradually from 99.2% of the initial sample without washing to 97.5% after 2-cyclic washing, and further to 92.2% after 4-cyclic washing, retaining more than 92% of the initial performance even after four consecutive washing cycles. At earlier time points, the bactericidal efficiencies were maintained above 83% throughout all four-washing cycles. These results demonstrate that the bactericidal activity of the Cu/Zn imidazolate fabrics is well preserved under repeated washing conditions, confirming their practical durability and reusability.

3.6 Adhesion and viability of bacteria on MOF-grown fabric

The viability of *E. coli* adhered to the fabric was assessed to elucidate the combined effects of surface anti-adhesion and ROS-mediated bactericidal activity at the solid–liquid interface. The calibration method correlating ATP luminescence and PI fluorescence signals with bacterial concentrations (CFU) is presented in Fig. S7. Absolute cell counts of live and dead *E. coli* adhered to the fabrics as a function of incubation time are shown in Fig. S8, and these values are combined in Fig. 6a to depict the relative viability within the total adherent population.

On untreated cotton fabric, the total number of adhered bacteria increased continuously, with live cells remaining dominant, attributed to facile wetting and the absence of intrinsic bactericidal functionality. At an early incubation time of 15 min, all pore-activated MOF-grown fabrics exhibited substantially reduced bacterial adhesion compared with their unactivated counterparts. Specifically, the adhered bacterial densities on ZIF-L_{act}, Cu : Zn$[1:1]_{act}$, and Cu : Zn$[3:1]_{act}$ were

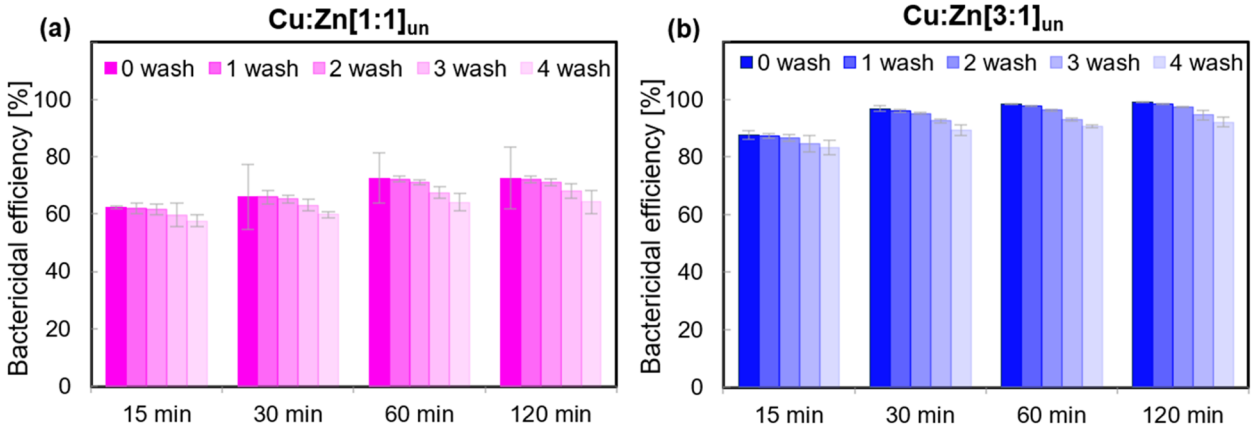

Fig. 5 Antibacterial durability of Cu/Zn imidazolate fabrics after repeated washing cycles. Bactericidal efficiency of (a) Cu : $Zn[1:1]_{un}$ and (b) Cu : $Zn[3:1]_{un}$ measured after repeated washing cycles using the ATP assay.

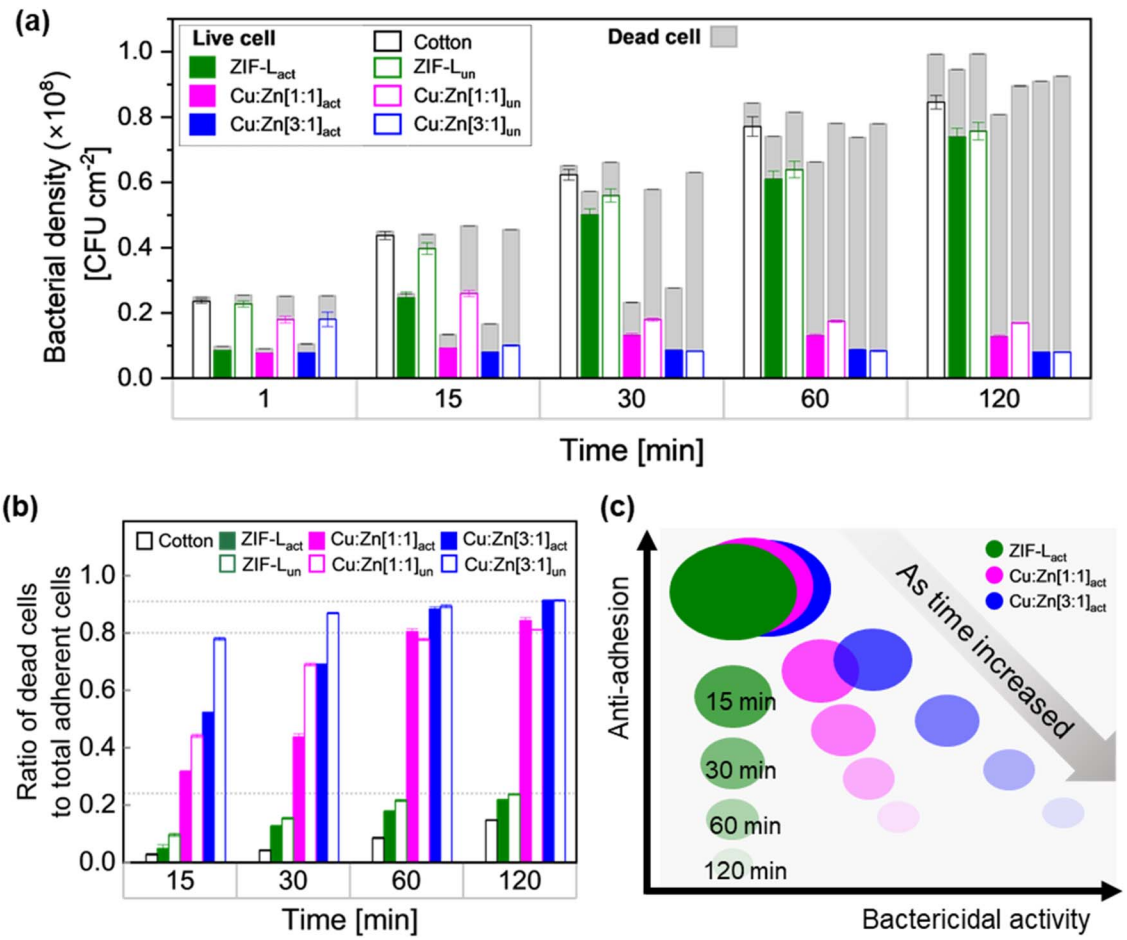

Fig. 6 (a) Relative cell viability within the adherent bacterial population. (b) Surface bactericidal efficiency expressed as the dead-cell fraction among adhered bacteria. (c) Schematic overview illustrating the sequential dual-defense antibacterial strategy, integrating initial anti-adhesion and subsequent bactericidal action.

approximately 0.26×10^8 CFU cm^{-2}, 0.13×10^8 CFU cm^{-2}, and 0.17×10^8 CFU cm^{-2}, corresponding to 59%, 29%, and 36% of the adhesion observed on their respective unactivated samples. This pronounced suppression of initial adhesion is attributed to effective inhibition of bacterial adhesion by the air-trapped superhydrophobic surface.

Until 30 min of incubation, the pore-activated Cu-containing MOF samples, Cu : $Zn[1:1]_{act}$ and Cu : $Zn[3:1]_{act}$, preserved

their anti-adhesive advantage, exhibiting only 40% and 44% of the adhesion levels of their respective unactivated samples. In contrast, ZIF-L_{act} displayed a significant rise in adhesion within 30 min, reaching 87% of that on ZIF-L_{un}. With further incubation to 60 min, the disparity in total adhesion between activated and unactivated samples significantly diminished for all samples, signaling the onset of a wetting transition. At this stage, the total adherence of ZIF-L_{act}, Cu : Zn$[1:1]_{act}$, and Cu : Zn$[3:1]_{act}$ reached 91%, 85%, and 95% of their respective unactivated samples. This convergence indicates wetting transition occurred by penetration of the bacterial suspension into the MOF pores, thereby eliminating the initial anti-adhesion effect of the air-trapped superhydrophobic state.

Despite this convergence in total adhesion, bacterial viability differed substantially depending on the MOF composition. Consistent with the wettability behavior, ZIF-L_{act} underwent wetting at the earliest stage (15 min), resulting in a rapid rise in total adhesion dominated by live cells, confirming its limited bactericidal activity. Conversely, the Cu-containing MOF fabrics displayed noticeable bactericidal effects. Although Cu : Zn$[3:1]_{act}$ showed slightly higher total adhesion than Cu : Zn$[1:1]_{act}$ across all time points, it accumulated a greater fraction of dead cells, consistent with its higher ROS generation capability as shown in Fig. 3a and b. The comparative bactericidal performance is summarized in Fig. 6b as the fraction of dead cells relative to the total adherent population. Cotton and ZIF-L samples maintained consistently low dead-cell fractions (<24%), while Cu : Zn$[1:1]_{act}$ reached approximately 80% dead cells after 60 min. Notably, Cu : Zn$[3:1]_{act}$ exceeded 50% dead cells within 15 min, and progressively increased to about 91% after 120 min.

As an integrated overview, Fig. 6c schematically illustrates the sequential dual-defense strategy of the MOF-grown fabrics. In the initial stage, the air-trapping layer formed by Cu/Zn imidazolate frameworks minimizes contact between the fabric and the bacterial suspension during short-term exposure, thereby effectively suppressing bacterial attachment to the fabric surface. With prolonged exposure, a wetting transition occurs as liquid infiltrates the MOF pores, activating interactions with bacteria and ROS-active sites on the fabrics and triggering ROS-mediated bactericidal activity. These time-sequenced events allow a seamless integration of anti-biofouling and bactericidal functions, harnessing wetting dynamics as a material design principle for a wettability-adaptive antibacterial system that provides dual-mode, sustained protection under prolonged bacterial exposure.

4. Conclusions

Cu/Zn bimetallic imidazolate frameworks with varying Cu/Zn ratios were grown on a cotton fabric, aiming to construct a fabric interface with dual-mode antibacterial function with antibiofouling and bactericidal activity. Beyond the specific antibacterial performance demonstrated here, this work establishes a materials design principle in which interfacial wetting dynamics are deliberately harnessed to program sequential functionality. The integration of anti-adhesion with ROS-mediated sterilization solves the intrinsic trade-offs of conventional antibacterial coatings by decoupling immediate antifouling protection from long-term bactericidal activity. Central to this design is the wetting transition, which operates as a reversible functional switch between defense modes. The initial superhydrophobic state stabilizes air pockets trapped within the MOF pores, resisting bacterial attachment, while subsequent wetting activates latent Cu–N coordination sites, allowing sustained ROS ($^{\bullet}O_2^-$ and $^{\bullet}OH$) through Cu^+/Cu^{2+} redox cycling. This mechanism induces intracellular oxidative stress in *E. coli*, as confirmed by DCFH-DA assays. Importantly, compositional modulation of the Cu/Zn ratio offers tailorability to balance between antifouling and bactericidal potency. Cu-rich frameworks (Cu : Zn$[3:1]_{un}$) favor rapid post-wetting sterilization with a bactericidal efficiency of 99.2% after 120 min, suitable for high-risk clinical settings, whereas Zn-rich compositions (Cu : Zn$[1:1]_{act}$) extend the anti-adhesive state, aligning with requirements for daily-wear textiles. This work advances a dynamic, wettability-responsive materials paradigm, in which functionality is not fixed but evolves in response to operational conditions. Such an approach offers a broadly applicable strategy for designing effective hygiene materials with enhanced longevity, adaptability, and application-specific performance across healthcare, wearable protection, and environmental interfaces. Furthermore, the bactericidal functionality was well retained after repeated washing cycles, with Cu : Zn$[1:1]_{un}$ and Cu : Zn$[3:1]_{un}$ maintaining over 94% and 92% of their respective initial bactericidal efficiencies after four successive washings, underscoring the practical reusability of the proposed textile platform.

Author contributions

Sujin Jeong: writing – original draft, visualization, validation, methodology, investigation, formal analysis, data curation, and conceptualization. Kyeongeun Lee: writing – original draft, visualization, formal analysis, data curation. Sebin Lee: investigation, formal analysis, data curation. Jooyoun Kim: writing – original draft, validation, supervision, resources, project administration, investigation, funding acquisition, formal analysis, conceptualization.

Conflicts of interest

The authors declare there are no conflicts of interest.

Data availability

All data related to this publication are available either in the main manuscript or its supplementary information (SI). Supplementary information: detailed experimental methods, materials, and characterization, ROS measurements, quantification of live and dead cells attached to fabric surface, ICP-AES and TGA analyses; additional SEM images and calibration procedures for ATP and PI assays, and bacterial adhesion and viability data (Fig. S1–S10). SI video demonstrating water repellency behavior on pore-activated MOF-grown fabric

surfaces (Video S1) and immediate wetting on unactivated fabric surfaces (Video S2) (MP4). See DOI: https://doi.org/10.1039/d6ra01949h.

Acknowledgements

This work was supported by the National Research Foundation of Korea (NRF) grant funded by the Korea Ministry of Science and ICT (MSIT) (Grant No. RS-2024-00405333; RS-2025-00523094).

References

1 N. Karim, S. Afroj, K. Lloyd, L. C. Oaten, D. V. Andreeva, C. Carr, A. D. Farmery, I.-D. Kim and K. S. Novoselov, *ACS Nano*, 2020, **14**, 12313–12340, DOI: 10.1021/acsnano.0c05537.
2 Q. Qiu, S. Chen, Y. Li, Y. Yang, H. Zhang, Z. Quan, X. Qin, R. Wang and J. Yu, *Chem. Eng. J.*, 2020, **384**, 123241, DOI: 10.1016/j.cej.2019.123241.
3 Y. Xiao, J. Jiang, R. Cai, J. Fu, S. Xiang, S. Zhao, F. Fu, H. Diao and X. Liu, *Adv. Fiber Mater.*, 2024, **6**, 444–457, DOI: 10.1007/s42765-023-00365-6.
4 R. Ettlinger, A. V. Desai, H. L. J. Cheong, L. L. Major, T. K. Smith, A. B. Naden, J. Hilton, C. S. Adamson, A. R. Armstrong and R. E. Morris, *Adv. Funct. Mater.*, 2025, e13928, DOI: 10.1002/adfm.202513928.
5 J. Sun, Y. Fan, W. Ye, L. Tian, S. Niu, W. Ming, J. Zhao and L. Ren, *Chem. Eng. J.*, 2021, **417**, 128049, DOI: 10.1016/j.cej.2020.128049.
6 J. Xue, J. Zhang, M. Yuan, Y. Lv, Z. Chen and M. Wang, *Sep. Purif. Technol.*, 2024, **333**, 125863, DOI: 10.1016/j.seppur.2023.125863.
7 J. Zhou, Z. Hu, F. Zabihi, Z. Chen and M. Zhu, *Adv. Fiber Mater.*, 2020, **2**, 123–139, DOI: 10.1007/s42765-020-00047-7.
8 A. Kumar, A. Sharma, Y. Chen, M. M. Jones, S. T. Vanyo, C. Li, M. B. Visser, S. D. Mahajan, R. K. Sharma and M. T. Swihart, *Adv. Funct. Mater.*, 2021, **31**, 2008054, DOI: 10.1002/adfm.202008054.
9 P. Natsathaporn, G. Herwig, S. Altenried, Q. Ren, R. M. Rossi, D. Crespy and F. Itel, *Adv. Fiber Mater.*, 2023, **5**, 1519–1533, DOI: 10.1007/s42765-023-00291-7.
10 J. Ma, Y. Sun, K. Gleichauf, J. Lou and Q. Li, *Langmuir*, 2011, **27**, 10035–10040, DOI: 10.1021/la2010024.
11 A. T. Krawczynska, A. Michalicha, P. Suchecki, K. Budniak, A. Roguska, M. Kerber, D. Setman, M. Spychalski, B. Adamczyk-Cieslak and M. O. Liedke, *Sci. Rep.*, 2024, **14**, 24549, DOI: 10.1038/s41598-024-75045-5.
12 H. R. Hong, J. Kim and C. H. Park, *RSC Adv.*, 2018, **8**, 41782–41794, DOI: 10.1039/C8RA08310J.
13 Q. Wang, M. Qiu, S. Yu, X. Yang, L. Lao, Z. Wu, Q. Deng and M. Yu, *J. Mater. Sci.*, 2024, **59**, 289–303, DOI: 10.1007/s10853-023-09200-0.
14 H. Qian, M. Li, Z. Li, Y. Lou, L. Huang, D. Zhang, D. Xu, C. Du, L. Lu and J. Gao, *Mater. Sci. Eng., C*, 2017, **80**, 566–577, DOI: 10.1016/j.msec.2017.07.002.
15 Y. Yuan, M. P. Hays, P. R. Hardwidge and J. Kim, *RSC Adv.*, 2017, **7**, 14254–14261, DOI: 10.1039/C7RA01571B.
16 D. Ashok, S. Cheeseman, Y. Wang, B. Funnell, S. F. Leung, A. Tricoli and D. Nisbet, *Adv. Mater. Interfaces*, 2023, **10**, 2300324, DOI: 10.1002/admi.202300324.
17 S. Chen, X. Li, Y. Li and J. Sun, *ACS Nano*, 2015, **9**, 4070–4076, DOI: 10.1021/acsnano.5b00121.
18 M. Klicova, Z. Oulehlova, A. Klapstova, M. Hejda, M. Krejcik, O. Novak, J. Mullerova, J. Erben, J. Rosendorf and R. Palek, *Mater. Des.*, 2022, **217**, 110661, DOI: 10.1016/j.matdes.2022.110661.
19 H. Zhou, H. Wang, T. Lin and H. Niu, *Mater. Des.*, 2021, **211**, 110145, DOI: 10.1016/j.matdes.2021.110145.
20 H. Zhou, H. Wang, H. Niu, A. Gestos and T. Lin, *Adv. Funct. Mater.*, 2013, **23**, 1664–1670, DOI: 10.1002/adfm.201202030.
21 H. Zhou, Q. Li, Z. Zhang, X. Wang and H. Niu, *Adv. Fiber Mater.*, 2023, **5**, 1555–1591, DOI: 10.1007/s42765-023-00297-1.
22 Z. Ye, S. Li, S. Zhao, L. Deng, J. Zhang and A. Dong, *Chem. Eng. J.*, 2021, **420**, 127680, DOI: 10.1016/j.cej.2020.127680.
23 H. R. Hong and J. Kim, *ACS Appl. Nano Mater.*, 2023, **6**, 18518–18530, DOI: 10.1021/acsanm.3c04015.
24 G. Vasiliev, A.-L. Kubo, H. Vija, A. Kahru, D. Bondar, Y. Karpichev and O. Bondarenko, *Sci. Rep.*, 2023, **13**, 9202, DOI: 10.1038/s41598-023-36460-2.
25 R. A. Gonçalves, J. W. Ku, H. Zhang, T. Salim, G. Oo, A. A. Zinn, C. Boothroyd, R. M. Tang, C. L. Gan and Y.-H. Gan, *ACS Appl. Nano Mater.*, 2022, **5**, 12876–12886, DOI: 10.1021/acsanm.2c02736.
26 A. Farouk, S. E.-S. Saeed, S. Sharaf and M. Abd El-Hady, *RSC Adv.*, 2020, **10**, 41600–41611, DOI: 10.1039/D0RA07544B.
27 K. Wang, M. Lv, T. Si, X. Tang, H. Wang, Y. Chen and T. Zhou, *J. Hazard. Mater.*, 2024, **461**, 132479, DOI: 10.1016/j.jhazmat.2023.132479.
28 T. D. Doan, N.-N. Vu, T. L. G. Hoang and P. Nguyen-Tri, *Coord. Chem. Rev.*, 2025, **523**, 216298, DOI: 10.1016/j.ccr.2024.216298.
29 B. Ran, L. Ran, Z. Wang, J. Liao, D. Li, K. Chen, W. Cai, J. Hou and X. Peng, *Chem. Rev.*, 2023, **123**, 12371–12430, DOI: 10.1021/acs.chemrev.3c00326.
30 Z. Zhou, B. Li, X. Liu, Z. Li, S. Zhu, Y. Liang and S. Cui, *ACS Appl. Bio Mater.*, 2021, **4**, 3909–3936, DOI: 10.1021/acsabm.0c01335.
31 X. Wang, H. Wang, J. Zhang, W. Ma, D. Zhang and Y. Chen, *J. Environ. Sci.*, 2025, **156**, 68–78, DOI: 10.1016/j.jes.2024.06.027.
32 X. Wang, H. Wang, J. Zhang, N. Han, W. Ma, D. Zhang, M. Yao, X. Wang and Y. Chen, *Nano Res.*, 2024, **17**, 7427–7435, DOI: 10.1007/s12274-024-6699-x.
33 M. Han, G. Liu and C. Zhu, *J. Membr. Sci.*, 2024, **708**, 123027, DOI: 10.1016/j.memsci.2024.123027.
34 M. S. Kim, S. Oh, W. Y. Kim, S. R. Park, S. N. Yoon, S. H. Choi, S. Shin, S. Kwon, K. Woo and S. Kim, *Appl. Surf. Sci.*, 2025, **682**, 161792, DOI: 10.1016/j.apsusc.2024.161792.
35 A. Schejn, A. Aboulaich, L. Balan, V. Falk, J. Lalevée, G. Medjahdi, L. Aranda, K. Mozet and R. Schneider, *Catal. Sci. Technol.*, 2015, **5**, 1829–1839, DOI: 10.1039/C4CY01505C.

36 J. Guan, L. Wang, F. Xu and G. Ma, *Microchem. J.*, 2025, 114856, DOI: 10.1016/j.microc.2025.114856.
37 A. Deacon, L. Briquet, M. Malankowska, F. Massingberd-Mundy, S. Rudić, T. L. Hyde, H. Cavaye, J. Coronas, S. Poulston and T. Johnson, *Commun. Chem.*, 2022, **5**, 18, DOI: 10.1038/s42004-021-00613-z.
38 S. Cong, S. Sun, Y. Zhang, M. Wang, Z. Jia, Y. Zhao and H. Pang, *Adv. Funct. Mater.*, 2025, e15548, DOI: 10.1002/adfm.202515548.
39 A. R. Talosig, F. Wang, J. T. Mulvey, B. P. Carpenter, E. M. Olivas, B. B. Katz, C. Zhu and J. P. Patterson, *Cryst. Growth Des.*, 2024, **24**, 4136–4142, DOI: 10.1021/acs.cgd.4c00194.
40 Y. Lo, C. H. Lam, C.-W. Chang, A.-C. Yang and D.-Y. Kang, *RSC Adv.*, 2016, **6**, 89148–89156, DOI: 10.1039/C6RA19437K.
41 X. Wang, H. Wang, J. Cheng, H. Li, X. Wu, D. Zhang, X. Shi, J. Zhang, N. Han and Y. Chen, *Chem. Eng. J.*, 2023, **466**, 143201, DOI: 10.1016/j.cej.2023.143201.
42 L. Li, L. Cao, X. Xiang, X. Wu, L. Ma, F. Chen, S. Cao, C. Cheng, D. Deng and L. Qiu, *Adv. Funct. Mater.*, 2022, **32**, 2107530, DOI: 10.1002/adfm.202107530.
43 P. Li, J. Li, X. Feng, J. Li, Y. Hao, J. Zhang, H. Wang, A. Yin, J. Zhou and X. Ma, *Nat. Commun.*, 2019, **10**, 2177, DOI: 10.1038/s41467-019-10218-9.
44 Q. V. Vo, L. T. T. Thao, T. D. Manh, M. Van Bay, B.-T. Truong-Le, N. T. Hoa and A. Mechler, *RSC Adv.*, 2024, **14**, 27265–27273, DOI: 10.1039/D4RA05437G.
45 Y. Sheng, I. A. Abreu, D. E. Cabelli, M. J. Maroney, A.-F. Miller, M. Teixeira and J. S. Valentine, *Chem. Rev.*, 2014, **114**, 3854–3918, DOI: 10.1021/cr4005296.
46 Y. Yu, S. Zhu, B. Hu and G. Pan, *Adv. Funct. Mater.*, 2025, **35**, e11530, DOI: 10.1002/adfm.202511530.
47 P. Makvandi, C. Y. Wang, E. N. Zare, A. Borzacchiello, L. N. Niu and F. R. Tay, *Adv. Funct. Mater.*, 2020, **30**, 1910021, DOI: 10.1002/adfm.201910021.
48 Y. Sang, F. Cao, W. Li, L. Zhang, Y. You, Q. Deng, K. Dong, J. Ren and X. Qu, *J. Am. Chem. Soc.*, 2020, **142**, 5177–5183, DOI: 10.1021/jacs.9b12873.
49 L. Zhao, Y. Chen, Q. Wei, X. Lv, Y. Cui, W. Wang, X. Mou, X. Song, X. Dong and Y. Cai, *Chem. Eng. J.*, 2024, **492**, 152265, DOI: 10.1016/j.cej.2024.152265.
50 I. Lee, J. Kim, R. Kwak and J. Lee, *Adv. Funct. Mater.*, 2023, **33**, 2213650, DOI: 10.1002/adfm.202213650.
51 D. Yu, Y. Zha, Z. Zhong, Y. Ruan, Z. Li, L. Sun and S. Hou, *Sens. Actuators, B*, 2021, **339**, 129878, DOI: 10.1016/j.snb.2021.129878.
52 Y. Zhang, S. Cai, X. Li, L. Zhang, M. Li, Y. Zhang, X. Wang and N. Zhou, *ACS Appl. Nano Mater.*, 2024, **7**, 22843–22854, DOI: 10.1021/acsanm.4c04025.